Reflooding of degraded cores in ASTEC V2.1: modelling and validation on PEARL experiments

Ignacio Gómez-García-Toraño, Laurent Laborde, Florian Fichot, Hervé Mutelle

HAL Id: hal-03863989

https://hal.science/hal-03863989

Submitted on 21 Nov 2022

Reflooding of degraded cores in ASTEC V2.1: modelling and validation on PEARL experiments

Authors and affiliations:

Ignacio Gómez-García-Toraño, Laurent Laborde (*), Florian Fichot

Institut de Radioprotection et de Sûreté Nucléaire, Service des Accidents Majeurs (SAM)

BP 3 - 13 115 Saint Paul lez Durance Cedex, France

***corresponding author (email: laurent.laborde@irsn.fr, phone: +33 442 19 95 16

Hervé Mutelle

Institut de Radioprotection et de Sûreté Nucléaire, Service d'études et de Recherches Expérimentales (SEREX)

BP 3 - 13 115 Saint Paul lez Durance Cedex, France

Abstract

The injection of water into the reactor vessel at a late stage of a severe accident (core reflooding) is one of the key Severe Accident Management measure to stop the progression of the accident in Light Water Reactors. Therefore, an appropriate modelling of the physical phenomena involved in this process is of paramount importance for the enhancement of safety of these nuclear power plants.

This article presents the improvements performed in the ASTEC V2.1 integral severe accident code in order to obtain a comprehensive reflooding model, which is valid regardless the core damage state. The main development consists in replacing, in presence of debris, the single momentum conservation equation (plus the drift flux relation) by two momentum conservation equations (one for each phase) with specific porous friction terms. Moreover, the calculation of the quench front position and the heat transfers downstream of the quench front have been harmonized.

The physical models are validated against experimental data from the PEARL facility where a large heated debris bed is quenched. A wide range of thermal-hydraulic (pressure, injection velocity) and geometrical parameters (bed particle diameter and bypass thickness) is investigated. Generally, ASTEC V2.1 provides a good agreement for tests involving either a one or two-dimensional quench front progression. However, conversion ratios of produced steam to injected water seem to be overestimated in two-dimensional tests with fine particle diameters, which raises questions about the modelling of capillarity in those situations.

The validated version of the code is then used to gain further insights on degraded core reflooding: radial steam redistribution is mainly driven by the large pressure gradients generated within the bed, whereas water entrainment is driven by the interfacial drag between the redistributed steam and the liquid, both contributing to hinder the coolability of the debris bed.

Keywords: ASTEC, severe accident, core reflooding, PEARL

Highlights

Each point must have a maximum length of 85 characters (including spaces). Write 3-5 bulleted points.

- Comprehensive reflooding model has been developed in ASTEC V2.1.
- Model is validated against PEARL experiments data on degraded core reflooding.
- Wide range of thermalhydraulic and geometrical parameters has been considered.
- ASTEC V2.1 can predict experiments involving both 1D/2D quench front progression.
- Capillarity may be playing an important role in tests with 2 mm particle diameters.

1   Introduction

Core cooling conditions in a Light Water Reactor can be significantly impaired by an uncontrolled initiating event together with the failure of the emergency core cooling systems. Insufficient cooling of the core for an extended time will result in an overheating of the fuel elements, which will eventually lead to the loss of integrity of the fuel rods (Schanz et al., 1992; Steinbrück et al., 2010). In a Pressurized Water Reactor (PWR), this event leads to the drainage of corium (mixture of molten materials) into the fuel assemblies and its downward relocation, in turn leading to the formation of accumulations of solid materials when corium freezes in colder parts of the core.

In this context, the injection of water into the reactor i.e. core reflooding is one of the most important Severe Accident Management (SAM) measures for PWRs to stop the progression of the accident (Hermsmeyer et al., 2014). However, the TMI-2 accident has shown that this action may also lead to further fragmentation of intact and degraded core structures, leading to the creation of debris beds with fragment size up to several millimeters (Broughton et al., 1989). If, on the other hand, cooling is not provided, accumulated molten materials will turn into a large molten pool, which will eventually reach the lower plenum. Upon interaction with water, the corium will fragment in particles of sizes up to few millimeters (Magallon, 2009), leading to the creation of debris beds with limited coolability. Hence, a thorough understanding of degraded core reflooding is crucial in order to predict if a given injection may succeed in quenching the core, which is the reason why it is one of the high-priority issues in severe accident research (Klein-Heßling et al., 2014).

The experimental database for debris bed reflooding mainly consists of tests dealing with top flooding (Cho et al., 1984; Ginsberg et al., 1986; Tung et al., 1984). Reflooding from the top is the most likely for debris beds formed in the reactor pit (especially for BWRs), which was extensively studied (Dhir, 1983). Nevertheless, experiments involving bottom flooding in one-dimensional and vertically stratified debris beds have been reported (Tung and Dhir, 1987; Tutu et al., 1984; Wang and Dhir, 1988). The more recent DEBRIS (Leininger et al., 2014; Schäfer et al., 2006) and PRELUDE (Bachrata, 2012) facilities have also contributed to broaden the experimental database. Generally, it is observed that coolability mostly depends on the mass flow rate, bed temperature and particle diameter, the quench front propagation being mainly one-dimensional. Additionally, multi-dimensional effects were clearly observed for experiments with (small) 1-2 mm particles and (high) 10 m/h injection velocities (Bachrata, 2012; Bachrata et al., 2013) as well as for experiments with a significant mass of Zircaloy-4, whose oxidation by steam drove temperatures above 1100 ºC in (Wang and Dhir, 1988). However, effects such as the bed configuration (particles, porosity, bypass),

bed size and system pressure have not been addressed yet (Hering et al., 2015). In this context, the recent PEARL experimental facility built at IRSN Cadarache has allowed to gain further insights on the coolability of a large-scale debris bed. The facility investigates for the first time the influence of the bypass (representing less-damaged zones at the core periphery) and the system pressure. Experimental results using a wide range of injection velocities, pressures and initial temperatures have been published (Chikhi et al., 2017; Chikhi and Fichot, 2017; Mutelle et al., 2017). The main conclusion is that low pressures, high initial temperatures and high injection velocities lead to a two-dimensional progression of the quench front and a decrease in the conversion ratio (ratio of steam mass generated to water mass injection), indicating a less efficient reflooding.

These experimental data are used to validate the physical laws of dedicated severe accident tools. Integral severe accident codes calculate the overall response of the nuclear power plant including the reactor coolant system, containment and source term to the environment. They include a combination of phenomenological and parametric models for the simulation of the relevant phenomena and must be fast-running tools for the simulation of a sufficient number of scenarios. As a result, they are generally used to support, develop and validate severe accident management programs. The integral severe accident ASTEC code, developed at IRSN (France), has made significant progress thanks to the development and validation of physical models within the European SARNET and CESAM-FP7 framework programs (Nowack et al., 2018; Van Dorsselaere et al., 2015), which in turn made possible the release of the V2.0 (Chatelard et al., 2014) and V2.1 series (Chatelard et al., 2016).

Particularly, ASTEC V2.1 provides a more consistent and enhanced description of the core thermalhydraulics through its CESAR module, which can now model two-dimensional two-phase flows using a five-equation numerical scheme (including one momentum equation for the mixture) and an empirical correlation for the drift flux. This approach has provided satisfactory results when describing the reflooding of intact cores (Gomez-Garcia-Torano and Laborde, 2021), but has led to poor validation results when dealing with the reflooding of porous media. The main reason for the deviations is that the use of a mixture momentum equation with a drift flux model assumes that the interfacial drag and buoyancy forces are much greater than regular friction terms (Bestion, 2011), which is not the case in porous media.

In this context, the present article describes the key modifications implemented in CESAR in order to describe two-phase flows in porous media and have a comprehensive reflooding model valid whatever the core degradation state. These modifications address the following aspects: first, detection of the degradation state of each mesh (intact or porous); second, resolution of the two

momentum conservation equations with specific terms of porous media when the mesh is porous; third, unification of heat transfer models in the quench front vicinity. The code physical models are then validated against data from the PEARL facility, including the experimental results involving different debris particle diameters and bypass widths. Eventually, code predictions are also applied to gain further insights on the physical phenomena observed in the experiment.

2 Modelling reflooding of intact vs. degraded cores in ASTEC V2.1

2.1 Presentation of ASTEC V2.1 code and CESAR module

The Accident Source Term Evaluation Code (ASTEC), developed at IRSN (France), simulates entire severe accident sequences in a nuclear water-cooled reactor from the initiating event to the eventual release of radioactive elements out of the containment. The code is mainly used for source term determination, SAMG and Level 2 Probabilistic Safety Assessment studies. It has a modular structure, each module dealing with a set of physical phenomena that may take place over the course of a severe accident. A detailed description of ASTEC V2.1 and its different modules can be found in (Chatelard et al., 2016).

The ICARE module deals with the thermal behavior and degradation of all vessel structures, whereas the CESAR module describes the thermalhydraulics in the reactor cooling system including the reactor pressure vessel. For such aim, CESAR uses a two-fluid and five-equation approach, although a six-equation resolution (not used in this study) has been recently implemented (Glantz et al., 2018). The mass and energy equations are solved at the center of the cell while the momentum equations are solved at the interfaces between connecting cells. Within the core region, the momentum equations are solved both at the axial and radial interfaces.

The five-equation numerical scheme together with the drift flux relation has provided reasonable results when describing the reflooding of intact and partially degraded core structures (Gomez-Garcia-Torano and Laborde, 2021). However, it has led to important deviations when analyzing degraded core reflooding, since this approach assumes that buoyancy and drag forces are much greater than regular friction terms (Bestion, 2011), which is not the case in porous media. In order to solve this problem, modifications have been implemented for the resolution of the momentum equation under the presence of porous media (section 2.2). In addition, the computation of heat fluxes in porous media has been modified in such a way that the reflooding model, already available for intact core regions, is now operational for degraded zones (see section 2.3). These modifications are included starting from the release of ASTEC V2.1.1.6.

2.2 New hydrodynamic model for porous media

The momentum equation on mean velocity classically used in the five-equation CESAR approach (plus a drift relation) is locally replaced, in presence of debris, by two momentum equations (one for each fluid phase) with specific porous friction. This new approach gives satisfactory results in cold debris beds (Gomez-Garcia-Torano et al., 2018). Considering the heterogeneity of the core degradation process, some regions may keep their integrity, whereas others may be fragmented or just melt and relocate at lower parts of the vessel. To treat such situations, CESAR compares at each time step the friction surface of remaining rods and debris (if any) in each mesh in order to define the mesh configuration as "bundle" or "porous". Then, it sets a friction flag over each junction interconnecting two meshes. The following situations may arise:

- Two adjacent porous meshes: calculation of hydrodynamics using six-equation scheme for porous media.

- Two bundle meshes: calculation of hydrodynamics using the five-equation scheme without considering specific friction terms of porous media.

- One porous mesh but not the adjacent one: in this case the code considers a porous media on half of the porous mesh and bundle frictions on half of the non-porous mesh.

The article focuses on the description of the first point. Assuming that convective terms are negligible in comparison to the rest of friction terms, the momentum conservation equation for the gas and liquid phases is described by Eq. 1 and Eq. 2. The first term at the left-hand side of the equation represents the hydrostatic pressure loss. Concerning the right-hand side of the equation, the first and second terms represent the viscous and inertial regular friction between the fluid k (gas: G or liquid: L) and the porous media (regular friction terms), whereas the third term represents the interfacial drag.

$$-(\nabla P_G + \rho_G g) = \frac{\mu_G}{KK_G} j_G + \frac{\rho_G}{\eta\eta_G} j_G \; |j_G| + \frac{F_i}{\alpha} \qquad \text{Eq. 1}$$

$$-(\nabla P_L + \rho_L g) = \frac{\mu_L}{KK_L} j_L + \frac{\rho_L}{\eta\eta_L} j_L \; |j_L| - \frac{F_i}{1-\alpha} \qquad \text{Eq. 2}$$

Here, ∇P_k is the pressure gradient, α is the void fraction; ρ_k and μ_k are the density and kinematic viscosity of the k-fluid respectively; g is the gravitational acceleration vector (null for horizontal junctions). The quantity j_k is the superficial velocity of the k-fluid. It is expressed as a function of the

interstitial velocity v_k using Eq. 3, where ε represents the medium porosity and α_k the volumetric fraction of the k-phase.

$$j_k = \frac{v_k}{\varepsilon \cdot \alpha_k}$$ Eq. 3

The geometry of the porous media is considered in the permeability K and the passability η. The smaller effective cross section of the k-fluid in the two-phase flow is considered in the relative permeability and passability K_k and η_k. The interfacial drag between the fluid phases is represented by F_i. The absolute permeability K and absolute passability η, in case of uniform spherical particles, are correlated with the particle diameter d_p and the porosity ε by the Carman-Kozeny relation and the Ergun law, with Ergun constants $h_K = 180$ and $h_\eta = 1.75$ as in (Bachrata, 2012).

$$K = \frac{d_p^2 \varepsilon^3}{h_K(1-\varepsilon)^2}$$ Eq. 4

$$\eta = \frac{d_p \varepsilon^3}{h_\eta(1-\varepsilon)}$$ Eq. 5

Among the available expressions for the calculation of relative passabilities and permeabilities listed in (Chikhi et al., 2016), the Reed formulation has been selected.

$$K_G = \alpha^3$$ Eq. 6

$$\eta_G = \alpha^5$$ Eq. 7

$$K_L = (1-\alpha)^3$$ Eq. 8

$$\eta_L = (1-\alpha)^5$$ Eq. 9

The interfacial drag is calculated using the Schulenberg correlation (Schulenberg and Müller, 1987), where σ represents the surface tension.

$$F_i = 350\,\alpha\,(1-\alpha)^7 \frac{\rho_L K}{\sigma\eta} g(\rho_L - \rho_G)(\frac{j_G}{\alpha} - \frac{j_L}{1-\alpha})^2$$ Eq. 10

2.3 Unification of the heat transfers

The quench front (QF) detection and the heat flux calculation along the transition boiling region are now performed identically regardless if the mesh is considered intact or porous. The model is only dedicated for bottom flooding situations. The quench front is detected at the lowermost mesh, noted *IQF* hereafter, where the debris temperature exceeds $T_{sat}+5$. Hence, it depends on the wall

temperature and void fraction profile. The additional condition to be satisfied is that the debris temperature of the mesh *IQF+1* must exceed the minimum film boiling temperature T_{MFB}. Then, the heat flux along the transition boiling region is described by the EXPCHF model (Gomez-Garcia-Torano and Laborde, 2021), which establishes an exponential decrease of the heat flux from the critical heat flux over a characteristic length. This length is computed as a function of the capillarity length described in (Chikhi and Fichot, 2010), even in porous media.

Regarding the rest of boiling heat transfer mechanisms, nucleate boiling, generally occurring below the quench front, is calculated using (Thom et al., 1965), which establishes a heat flux dependency $(T_w - T_{sat})^2$, where T_w is the particle temperature. Film boiling, generally occurring above the T_{MFB} is evaluated using (Berenson, 1961), which establishes a dependency on $(T_w - T_{sat})^{3/4}$.

3 The PEARL experimental facility

The PEARL experimental facility at IRSN Cadarache (France) aims at improving the understanding of the factors governing the coolability of large heated debris beds. To present, experiments with a wide range of thermalhydraulic (system pressure, injection velocity and initial temperature), geometrical (debris particle diameter and bypass thickness) and injection positions have been performed. The current article only deals with bottom flooding tests.

3.1 Experimental setup and validation matrix

A complete description of the PEARL facility is available in (Chikhi and Fichot, 2017). Thus, only the main features of the test section and the instrumentation of the debris bed are recalled here. The test section is composed of a long quartz tube with an internal diameter of 540 mm. The debris bed, approximately 500 mm in height, is placed inside the quartz tube and is heated by an induction coil (see Figure 1). Water can be injected at the bottom or at the top, from a pressurized water tank. The steam flow, generated by the reflooding, is evacuated outside the building through a heated line equipped with a steam flow meter (Annubar flow meter). Pressure in the vessel is regulated by means of a pneumatic valve implemented at the end of the discharge line.
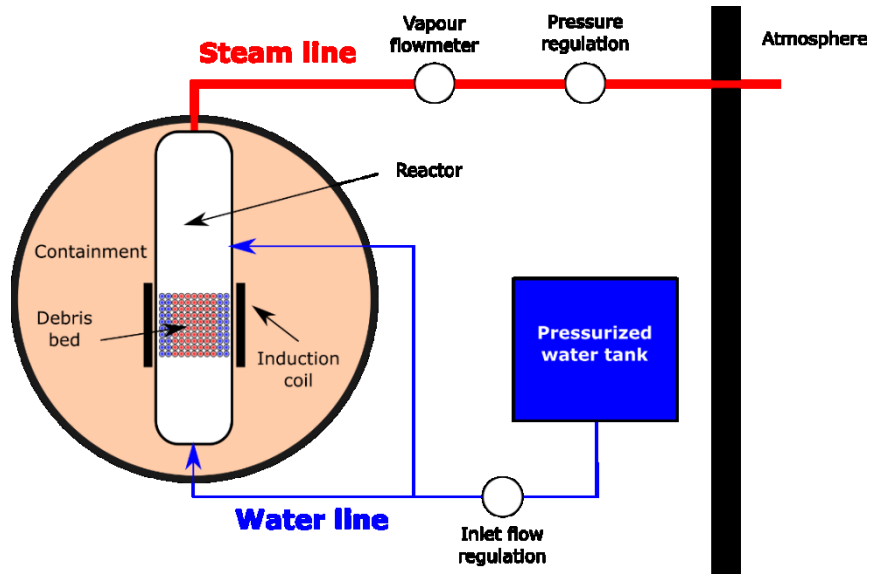
Figure 1: Schematic view of the PEARL facility.

The main bed (C) consists of stainless-steel balls and is surrounded by a bypass (BY) made of quartz balls (see Figure 2). A 100 mm high quartz bed (8 mm particles) is supporting the experimental debris bed. The purpose of the quartz region is to ensure a fully developed flow at the bottom of the heated debris bed. Likewise, a 100 mm high upper quartz bed (balls diameter 8 mm) is located above the bed. The debris bed is equipped with K-type thermocouples (diameter of 1 mm) implemented in the bed pores at different elevations along vertical axes distributed radially and at different angular positions.
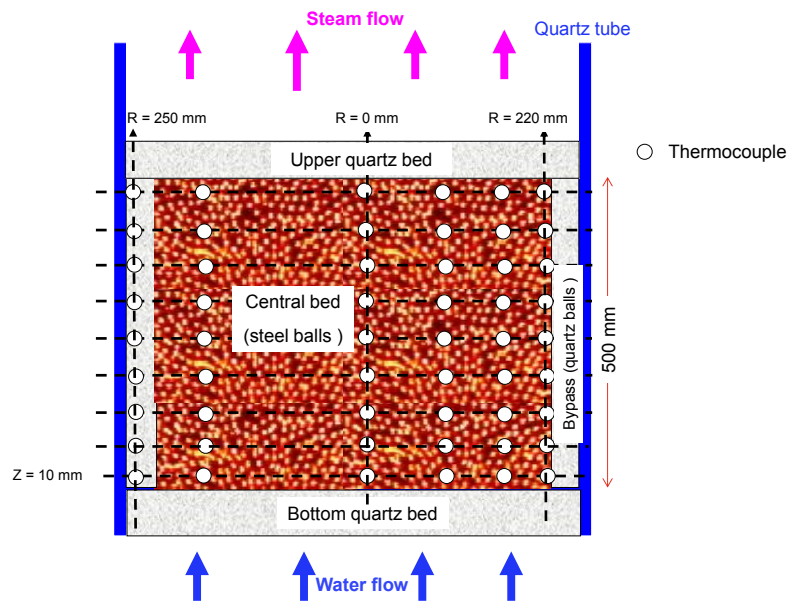

Figure 2: Debris bed structure and instrumentation. The radial positions of the instrumented vertical axis correspond to the values for the beds 1 and 2-1.

In bottom flooding experiments, the bed is subjected to successive heat-up phases via the induction furnace to reach the target initial temperature. Then, the furnace is stopped, and the water is injected into the bed. The furnace is then restarted when the water penetrates the bottom of the experimental bed, this being linked to a sharp rise of the steam generation rate. During all the reflooding time, the induction energy deposited in the steel balls bed with a specific power of 150 W/kg. This value is representative of the decay heat ten hours after SCRAM in a 1300 MWe PWR assuming that the entire core becomes a debris bed. Water injection and bed heating are stopped when the bed temperature falls below saturation.

Within this article, a wide range of experiments involving different system pressures (P), initial temperatures (T) and injection velocities (V_{inj}) has been selected. These have been carried out in three different debris beds (1, 2-1 and 2-2), each of which is characterized by the bed particle diameter (d_p^C) and bypass thickness (Th_{BY}). It is worth noting that the permeability and passability ratios between bypass and the main bed calculated from Eq. 4 and Eq. 5 remain the same regardless of the bed used ($K_{BY}/K_C = 4$, $\eta_{BY}/\eta_C = 2$).

The list of experiments used in this study is given in Table 1. Regarding test conditions, one can mention that the initial temperatures lying in the range 400-700 ºC are well below the 2000 ºC that can be expected in a debris bed. However, as far as the quenching of a debris bed is concerned, studies have shown that the behavior at 700 ºC is quite representative of the reality (Bachrata, 2012). Injection velocity is characteristic of the water flowrate delivered by a mobile pump injecting late in the accident. The system pressure, lower than 10 bar, covers the pressure conditions of a large part of nuclear accident scenarios during the fuel degradation (involving a primary side depressurization). The steel balls are designed to be as representative as possible of the porous media constituted by a real debris bed mixing fragmented fuel pellets and cladding particles. Therefore, the size and composition of particles was selected according to previous works on debris bed morphology (Akers et al., 1986; Coindreau et al., 2013), whereas the bypass thickness indicates that about 70-85 % of the radial space is blocked by the debris bed. The debris bed diameter was selected to be about 100 times larger than the size of particles, in order to detect any 2D effect. The height of the bed had to be of the same magnitude as the diameter, as expected in a debris bed of a degraded core.

Table 1: Selected PEARL experiments for the validation of the ASTEC V2.1 reflooding model. All selected experiments have been carried out with an initial debris bed temperature of 700°C.

Experiment	Bed	Mass of steel balls (kg)	P (bar)	V_{inj} (m/h)	d_p^C (mm)	Th_{BY} (mm)
PA-2	1	360	1	5	4	45
P3-3			3	2		
P3-10			3	5		
P5-1			5	5		
D1-7	2-1	378	1	5	2	45
D3-7			3	5		
D3-10			3	2		
D5-2			5	5		
BP3-1	2-2	457	3	5	2	20
BP3-2			3	2		
BP5-2			5	5		

The maximum measurements uncertainties for the PEARL facility is presented hereafter: injection flow rate (±4.6 % at 100 g/s and ±0.7 % at 700 g/s), steam flow rate at the outlet (± 9.8 % of the measured value), differential pressure between the top and the bottom of the quartz tube (0.56 mbar) and temperatures (±6°C at 100°C and ±9°C at 1000°C). Uncertainties have been expanded with a factor k=3, which corresponds to a confidence interval of 99.8%. In addition, the values mentioned include the uncertainty over the entire measurement chain (sensor, cables, conditioner (amplifier) and acquisition system). Uncertainty on quenching time of a given thermocouple is estimated +/-5s, and uncertainty on thermocouple location is 20mm.

3.2   Modelling the PEARL facility with ASTEC V2.1

The ASTEC V2.1 geometrical model of the test section is represented in Figure 3. The central bed (C) and the bypass (BY) are represented using red and blue particles, respectively. The bypass is radially surrounded by an adiabatic wall. This assumption is justified because the temperature of the bypass is generally close to saturation during reflooding. The upper quartz bed is included due to its non-negligible contribution to the total steam generation for each experiment, in contrast to the lower quartz bed. The central bed is radially divided in three channels of equal area, whereas the bypass is modeled with one channel. The bed is axially discretized in regions of 50 mm length (ten for the

central bed and two for the upper quartz bed). Discretizations with a higher refinement in the axial and radial direction have also been conducted, but the results remain similar to the ones presented in this article.

The water enters at the bottom of the central bed ($z = 0$ mm) with a constant mass flow rate, even if the experiments showed small fluctuations around the nominal value. The inlet water temperature is taken from the thermocouple located at the bypass at the elevation z=10 mm, since this value varies significantly during the experiment. These variations are due to the fact that the bottom layer of quartz balls is initially at a higher temperature than the water flow and thus exchange heat with the fluid. The pressure is set constant at the outlet of the facility, which is congruent with the pressure regulation during the experiment. The steel particles of the central bed are heated by induction according to the power experimental values, which are close to 150 W/kg.

A uniform initial temperature equal to the set-point of each experiment is assumed throughout the main debris bed. Likewise, the bypass is assumed to be at the saturation temperature at the system pressure. In fact, there are some heterogeneities, but their influence on the predictions has proved to be limited. In the experiments, liquid penetration in the heated bed is characterized by a sharp increase of the steam flowrate. That time is the t=0 s in all the simulations this allowing to set the initial liquid level at the bottom of the debris bed.
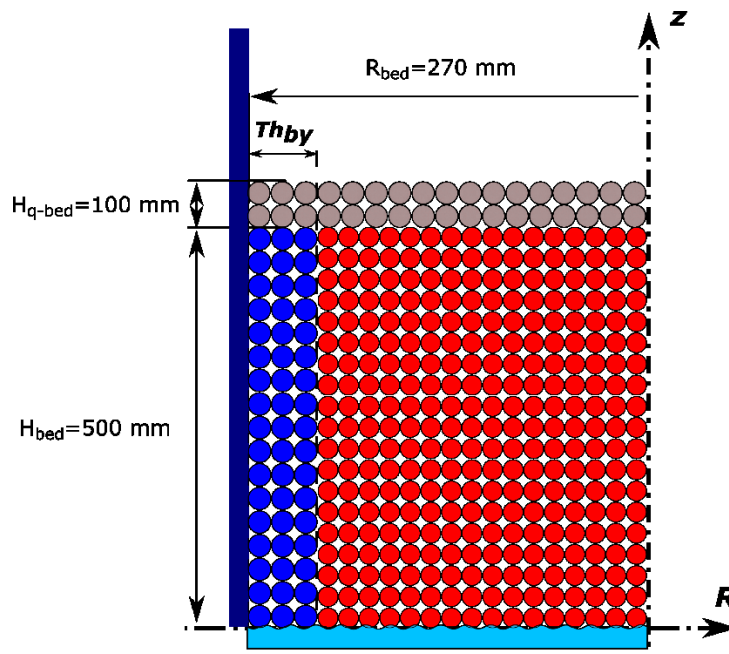

Figure 3: Axial view of the PEARL debris bed with ASTEC V2.1: red beads represent the heated central bed (C), blue beads represent the bypass (BY) and grey beads represent upper quartz bed (Q). The bottom of the central bed and bypass are located at z = 0 mm.

4 Validation of the reflooding model using PEARL experiments

4.1 Results on Bed 1 (D_P=4 mm, TH_{BY}=45 mm)

The comparison of the experimental and computational evolution of the quench front progression at different radii and the steam generation rate at the outlet are represented from Figure 4 to Figure 5 for selected tests. The predicted quench front progression along the bypass is not represented, since the method exposed in section 2.3 inhibits the calculation of the quench front when the debris temperature of the hypothetical mesh IQF+1 is higher than T_{MFB}. Since the bypass is assumed at saturation temperature at injection time, QF predictions along the bypass do not give a right representation of the behavior, which is the reason why they have been omitted from this study.

The comparison of the experimental data from PA-2 and P5-1 shows that a higher system pressure favors a one-dimensional progression of the quench front. Conversely, the reduction of the system pressure slows down the quench front progression across the main bed and speeds it up across the bypass. Water outflow from the bypass before the end of the complete quenching of the debris bed was confirmed by the video recording. As a result, there are two differentiated quench fronts: one along the bypass and one along the main heated bed. The same behavior is observed for high temperatures and injection velocities (Chikhi et al., 2017; Chikhi and Fichot, 2017; Mutelle et al., 2017). A careful look at the experimental quench front progression at R=220 mm (close to the bypass, see Figure 2) for PA-2 test shows that the reflooding time is lower at the top of the bed (z = 480 mm) than just below (z = 420 mm) suggesting the occurrence of top flooding. The steam generation rate shows a progressive increase in P5-1 because the upward one-dimensional quench front encounters progressively hotter regions, which have heated up since the start of water injection. Conversely, PA-2 shows a decrease of the steam generation rate followed by a plateau and a second peak.

Code predictions are in good agreement with the experimental data for both tests. Predictions slightly differ from experimental results in terms of the radial quench front profile for the test PA-2. Indeed, such profile is slightly flatter in ASTEC, as reflected in the proximity of the quench fronts at R=0mm and R=220 mm. In any case, the steady two-dimensional quench front progression (one in the bypass, one in the main bed) is captured for PA-2. For the test PA-2, the code correctly predicts a plateau in the steam generation rate during the progression of the quench front. Moreover, the initial and final peaks in the steam generation rate are also captured. Nevertheless, the qualitative behavior

of the steam generation rate is slightly different to the experiment since it experiences a sharp decrease at about 400 s and the peak is shifted in time. This aspect will be discussed in section 5.3.

One common point to all simulations is that the code predicts strong oscillations, which have their origin in the heat transfer associated with the reflooding model. In particular, when the quench front jumps from the mesh IQF to the IQF+1, the calculation of the heat flux applied in the mesh IQF switches from a specific modelling in the quench front mesh to a nucleate boiling correlation which can take very high values if debris are not yet cooled down to saturation temperature (see section 2.3). This switch generates a peak of steam production at each mesh boundary. Optimization efforts in the quench front tracking method are underway in order to smoothen the oscillations.
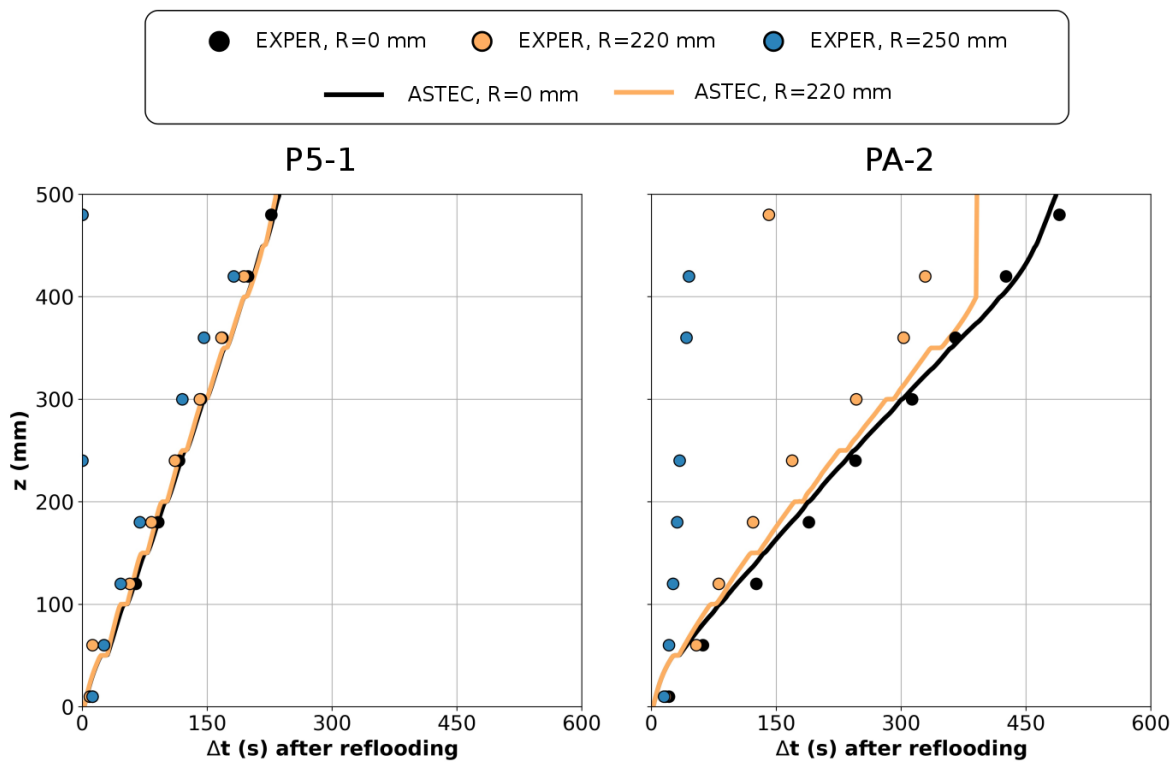

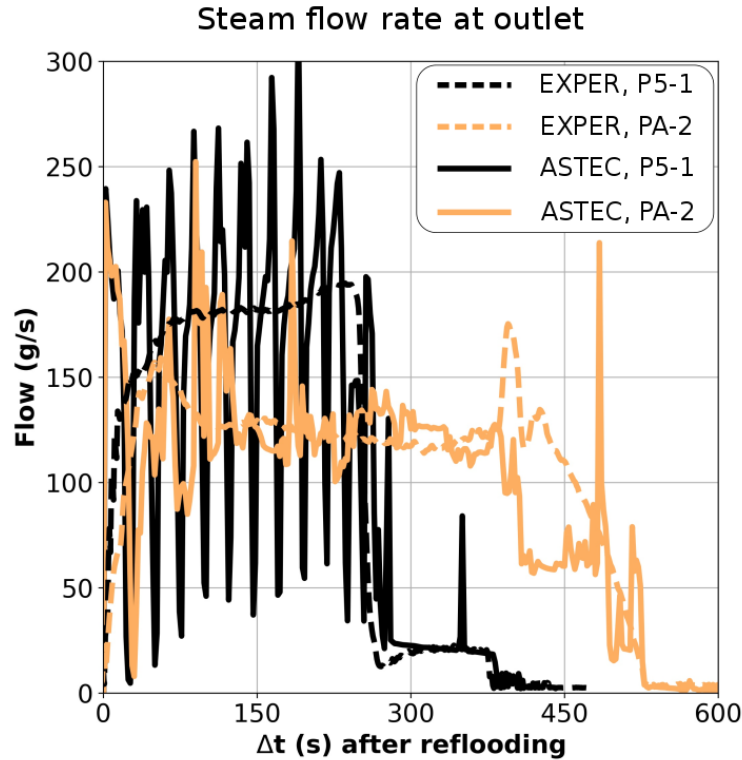Figure 4: Predicted vs. Experimental quench front evolution for the tests P5-1 and PA-2.

Steam flow rate at outlet

Figure 5: Predicted vs. Experimental evolution of the steam flow rate at the outlet for tests P5-1 and PA-2.

4.2 Results on Bed 2-1 (D_P=2 mm, Th_{BY}=45 mm)

The aim of this section is to study the particle diameter effect on the flow behavior. The tests D5-2 and D1-7 have been selected to evaluate the code response regarding the size of the particles since they allow a direct comparison with P5-1 and PA-2 (at 5 and 1 bar respectively). Likewise, the evolution of the quench front progression and the steam flow rate at the outlet are represented in Figure 6 and Figure 7.

A comparison between the experiments D5-2 and P5-1 shows that a reduction of the particle diameter reduces the quench front velocity in the center and enhances a non-uniform progression of water as a function of radius (multidimensional effects). These are more pronounced when the system pressure is 1 bar, as shown in D1-7. Indeed, it took 450 s/1200 s to quench the main bed in D5-2/D1-7, in contrast to the 210 s/470 s needed for P5-1/PA-2. The difference is not correlated to the mass of the central beds (see Table 1). Consequently, the quench front profile is more curved across the main bed. Another difference is that, despite the marked multi-dimensional behavior of D5-2 and D1-7, none of them indicates the existence of top flooding, which contrasts with PA-2 and other two-dimensional tests in Bed 1. Top flooding has not generally been observed in PEARL tests performed in Bed 2-1 and 2-2.

13

Both D5-2 and D1-7 show an initial peak in the steam generation rate followed by a progressive decrease in time, which contrasts with the two peaks and the plateau of PA-2. It is noticed that the reduction of the system pressure (from D5-2 to D1-7) leads to a decrease of the steam mass flow rate at the outlet for two reasons: first, part of the injected water is diverted to the bypass not contributing to debris bed quenching; second, the larger amount of water accumulated above the bed (not shown in the figures) enhances steam condensation. Both the disappearance of the second peak and the absence of top flooding will be further discussed in the section 5.3.

It can be concluded that the decrease of particle diameters enhances multi-dimensional effects for the same thermalhydraulic conditions, eventually increasing quenching time. However, this does not lead to an enhancement of top flooding according to the experimental data.

Alike the previous section, code predictions match experimental results regarding steam flowrate evolution and quench front velocity in the center of the bed. Nevertheless, it should be mentioned that code predictions tend to calculate a flatter quench front progression across the main bed than the marked multi-dimensional progression shown in the experiment. Furthermore, computational results show a vertical jump of the quench front at the end of reflooding, which means that the bottom quench front reaches a zone already cooled by top flooding. As pointed out previously, this is in contradiction with the experimental evidences on Bed 2-1. The radial heterogeneity in the quench front progression and the prediction of top flooding will be further analyzed later in section 5.3.
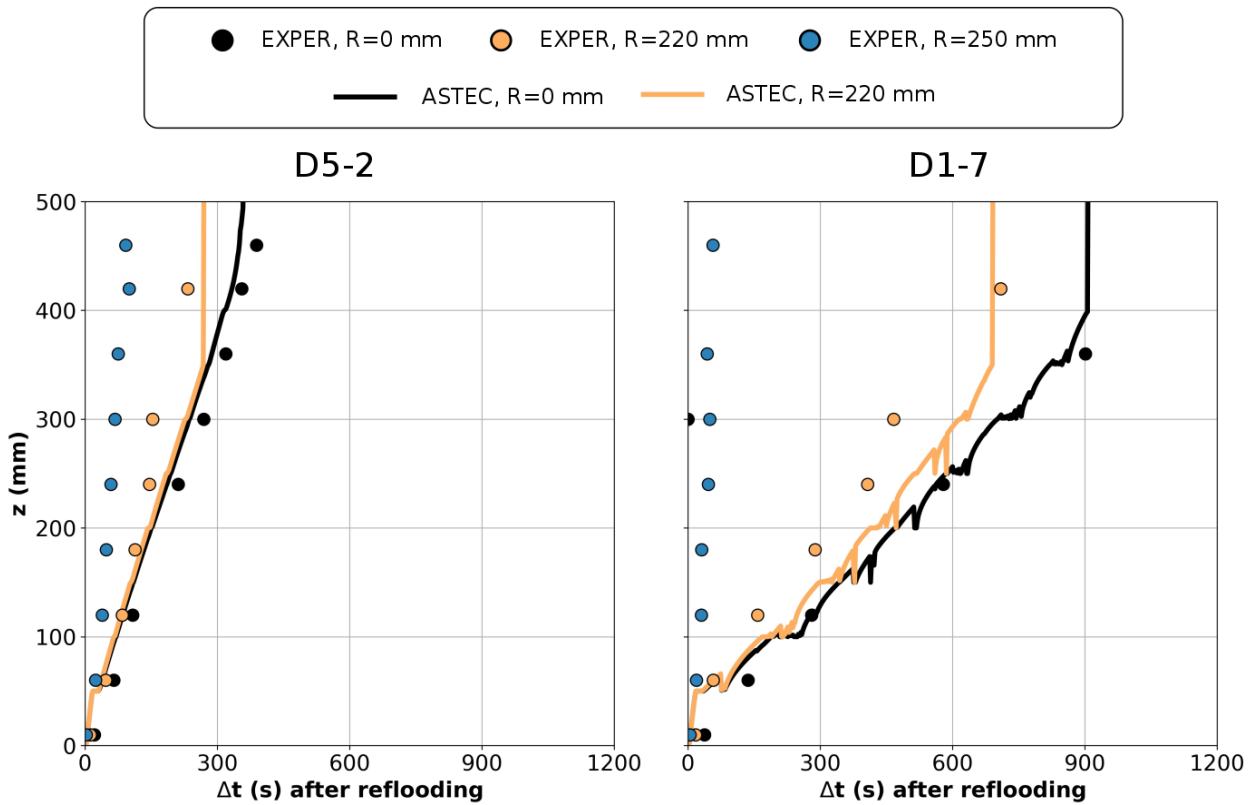
Figure 6: Predicted vs. Experimental evolution of the quench front for D5-2 (5 bar) and D1-7 (1 bar).
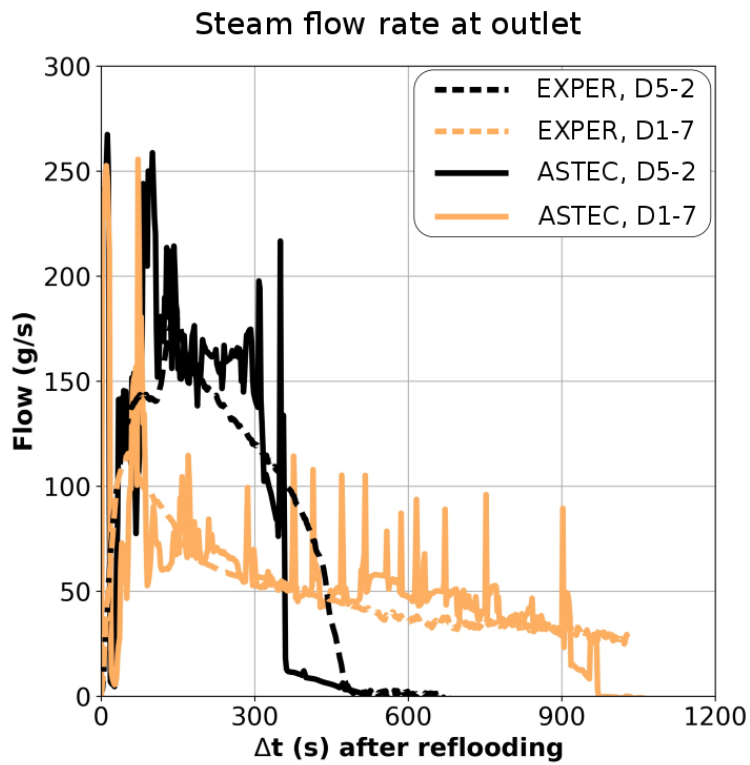

Figure 7: Predicted vs. Experimental evolution of steam flow rate at the outlet in D5-2 and D1-7.

15

4.3 Results on Bed 2-2 (D_p=2 mm, Th_{BY}=20 mm)

This part aims to study the bypass thickness effect on the flow behavior. In this section, the test BP5-2 is selected, since it allows a direct comparison with D5-2. The test BP3-1 is used to depict the influence of the pressure with respect to BP5-2. The evolution of the quench front at R=0 mm and the total steam mass associated with those tests are presented in Figure 8. The vertical lines in the quench front evolution give the time at which the predicted gas temperature outlet reaches saturation. This time is related to the arrival of water at the top of the bed.

In all tests, the gas outlet temperatures reach saturation much earlier than the arrival of the quench front at the top of the bed. This is linked to the steam redistribution towards the bypass, which enhances water entrainment, accumulation of water on top of the bed and the steam cooling. This mechanism is even more emphasized when decreasing the system pressure. Despite the enhancement of condensation at the top of the bed in those cases, the net steam generation is still significant because of the higher bed temperatures, which are the result of the lower quench front velocity within the main bed. A further analysis of D5-2 vs. BP5-2 reveals that the reduction of the bypass thickness increases the total steam mass produced, which is consistent with the increase of the mass of steel balls in the central bed, but it has hardly any effect on the quench front progression across the main bed. This aspect is discussed in the following section.

Generally, code predictions provide a good description of the experimental observations. However, the reflooding model presents the same deficiencies as those highlighted in the previous section for tests involving significant multi-dimensional effects: there is less availability of water in the bottom quenching process, but more availability in the top quenching process, which in turn reduces the peak temperature of the debris bed, since hottest regions are generally found at the top. This is clearly evidenced in Figure 9 showing the evolution of the experimental and computational debris bed temperatures at selected radial and axial locations for the test BP5-3. Indeed, code predictions show that the debris located at z > 460 mm is cooling down before the arrival of the bottom quench front, whereas experimental temperatures show the typical bottom quench behavior. A side consequence of predicting a lower average debris bed temperature during the transient is that less water needs to be evaporated to cool down the debris. This is coherent with the underestimation of the total steam mass at the end of the transient, not only for BP5-2, but also for D5-2 and BP3-1.

Therefore, for identical initial thermalhydraulic conditions, it can be concluded that an additional reduction of the bypass thickness enhances the steam generation but has hardly any effect on the quenching time of the main bed.
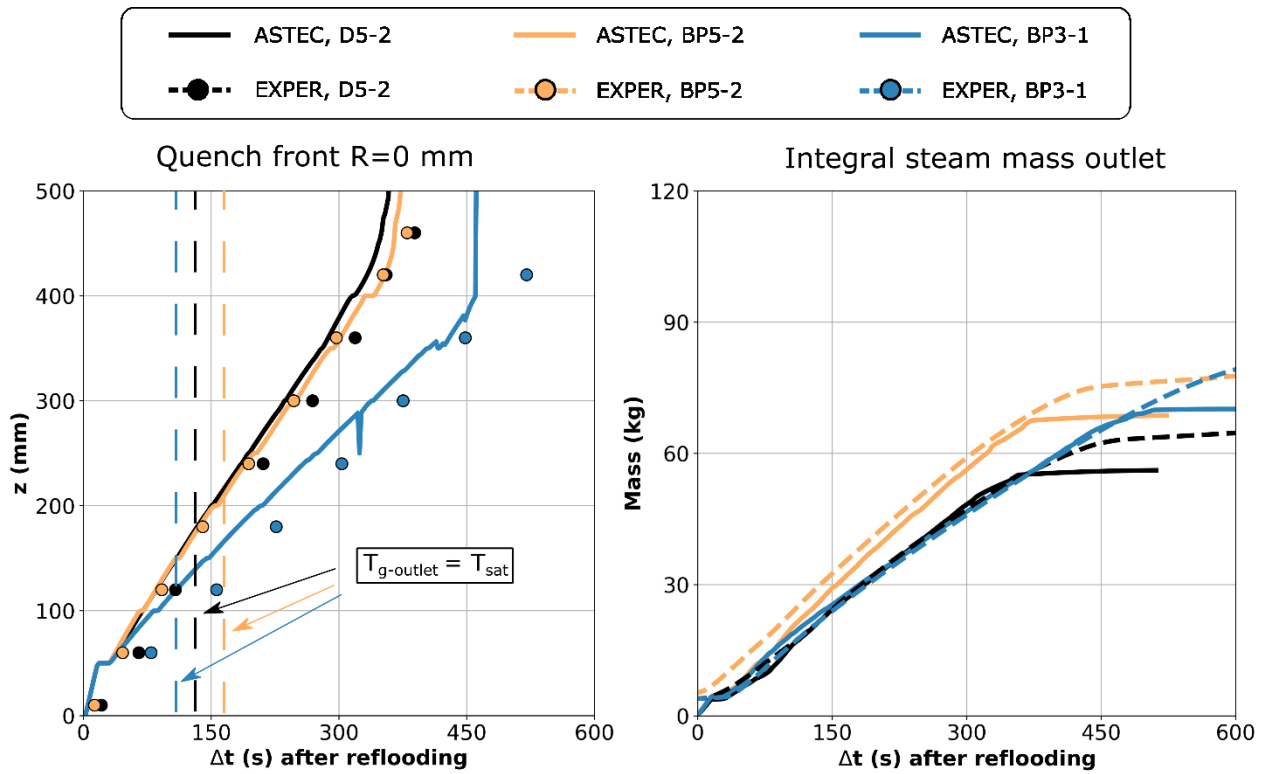
Figure 8: Predicted vs. Experimental evolution of the quench front evolution at R=0 mm and cumulated mass of steam at the outlet for the tests D5-2 and BP5-2 (5 bar, 700ºC, 5 m/h) and BP3-1 (3 bar, 700 ºC, 5 m/h).
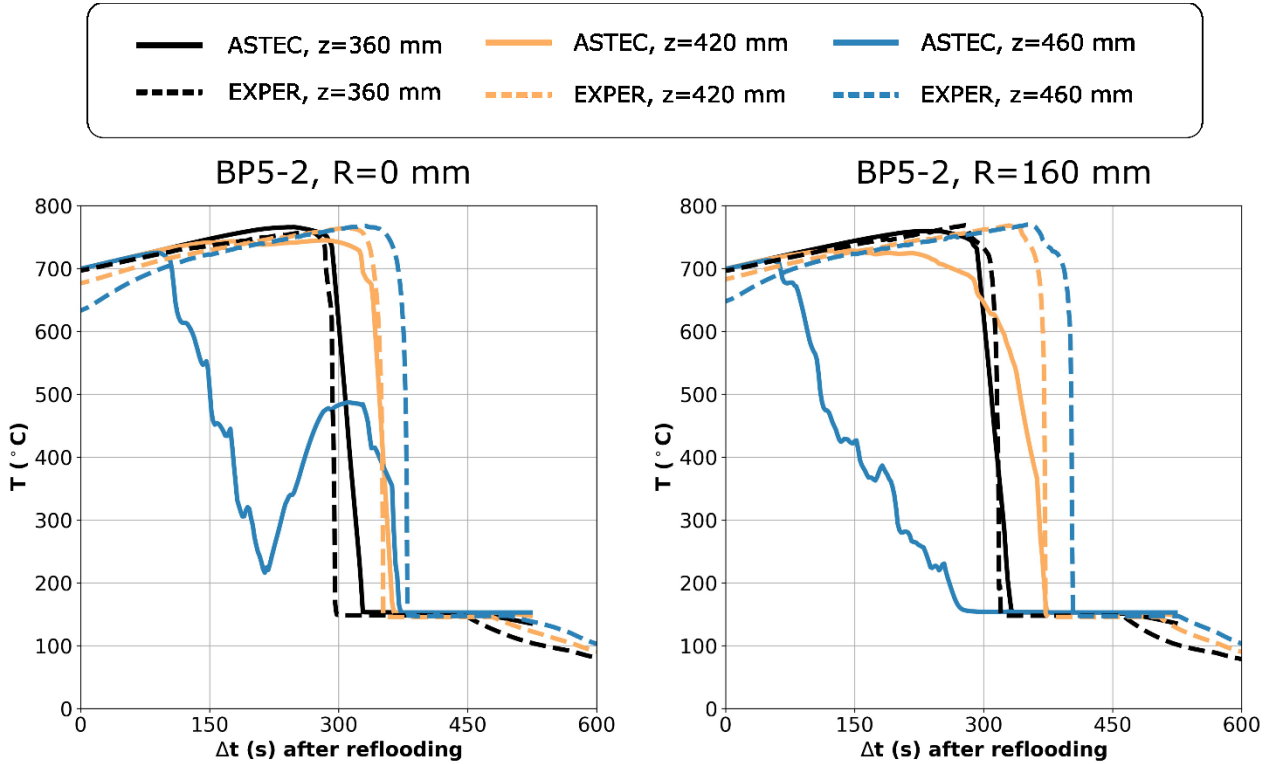

Figure 9: Evolution of computational and experimental debris temperatures at selected radial and axial locations for the test BP5-3.

17

4.4 Integration of all experimental campaigns

This section analyzes the combined effect of pressure, injection velocity and bed configuration for all PEARL tests with an initial temperature of 700 ºC, the results being entailed in Figure 10. Therein, the quench front velocity ratio (γ_u) and the conversion ratio (γ_{cr}) are represented as a function of the pressure (for an injection velocity of 5 m/h) and the injection velocity (for a system pressure of 3 bar). Here, γ_u is defined as the quench front velocity at R=0 mm divided by the apparent injection velocity (v_{inj}/ε), while γ_{cr} is defined as the steam mass flow rate at the outlet divided by the injection water flow rate (Chikhi and Fichot, 2017). Both variables are time-averaged during the reflooding phase. The sudden jump of the quench front to the top of the bundle is not considered in the calculation of the experimental and computational velocities. Points in the graph have two attributes: shape and color. The shape represents the geometrical features of the debris bed, whereas the color is used to distinguish experimental data from calculated results. There are no experimental data available for system pressure of 1 bar, injection velocity 5 m/h and initial debris temperature of 700 °C for Bed 2-2.

Previous studies at the PEARL facility already showed that the increase of the system pressure or the injection velocity contributed to reduce the quenching time up to a certain lower limit (Chikhi et al., 2017; Mutelle et al., 2017). However, pressure and injection velocity have opposite effects in terms of cooling efficiency. Indeed, an increase of the system pressure increases γ_u and hence γ_{cr}, this meaning that water is more efficiently used to cool down the debris bed. Conversely, the increase of the injection velocity decreases both γ_u and γ_{cr}. Hence, even if quenching time decreases with increasing velocities, the efficiency of reflooding is worsened in relative terms.

As explained in section 4.2, conversion and quench front velocity ratios decrease sharply when reducing the particle size. An additional reduction of the bypass thickness (see section 4.3) increases γ_{cr} because of the larger amount of heated mass and initial energy along the bed, but hardly impacts γ_u. This indicates that there is a bypass thickness for which two-dimensional effects are the most pronounced, this corresponding to maximum water entrainment. If the bypass thickness decreases below this value, the behavior tends to be one-dimensional. This was analytically shown in (Swaidan, 2018).

Code predictions provide a good description of γ_u whatever the bed configuration, system pressure, and injection velocity, even if the values are slightly underestimated with respect to the experimental ones. It should be kept in mind that γ_u provides information about the quench front progression at

R=0 mm but does not give the whole picture of the entire bed. This information can be deduced from γ_{cr}, whose qualitative prediction also presents a satisfactory agreement with the experimental tendencies. However, predictions tend to overestimate it for small particle beds.

At first glance, the simultaneous underestimation of γ_u and overestimation of γ_{cr} is a contradiction. Generally, the decrease of γ_{cr} (indicating a less efficient reflooding) is correlated with a decrease of γ_u (suggesting a slower quench front progression in the center), as pointed out previously. This is indeed what is happening in the simulations with bottom flooding: ASTEC predicts a flatter quench front across the bed than the experiment (as shown in previous sections), which in turn contributes to the decrease of γ_u and γ_{cr}. However, the occurrence of top flooding contributes to increase γ_{cr} without altering γ_u, bringing back to the bed some of the water entrained through the bypass. Consequently, the better prediction of γ_{cr} for decreasing system pressures is not the result of a better prediction of the phenomena, but the result of a compensation of the slow quench front progression across the central bed with a more significant top flooding (not observed in Bed 2-1 or Bed 2-2).

In conclusion, even if the quantitative agreement with the experimental data is satisfactory, the qualitative description of phenomena shows discrepancies (of minor impact on the global predictions) and developments are required to improve code predictions, especially for multi-dimensional tests performed on beds with $D_p < 2$ mm. In this sense, developments should aim at obtaining a more accurate prediction of the radial quench front profile across the bed.
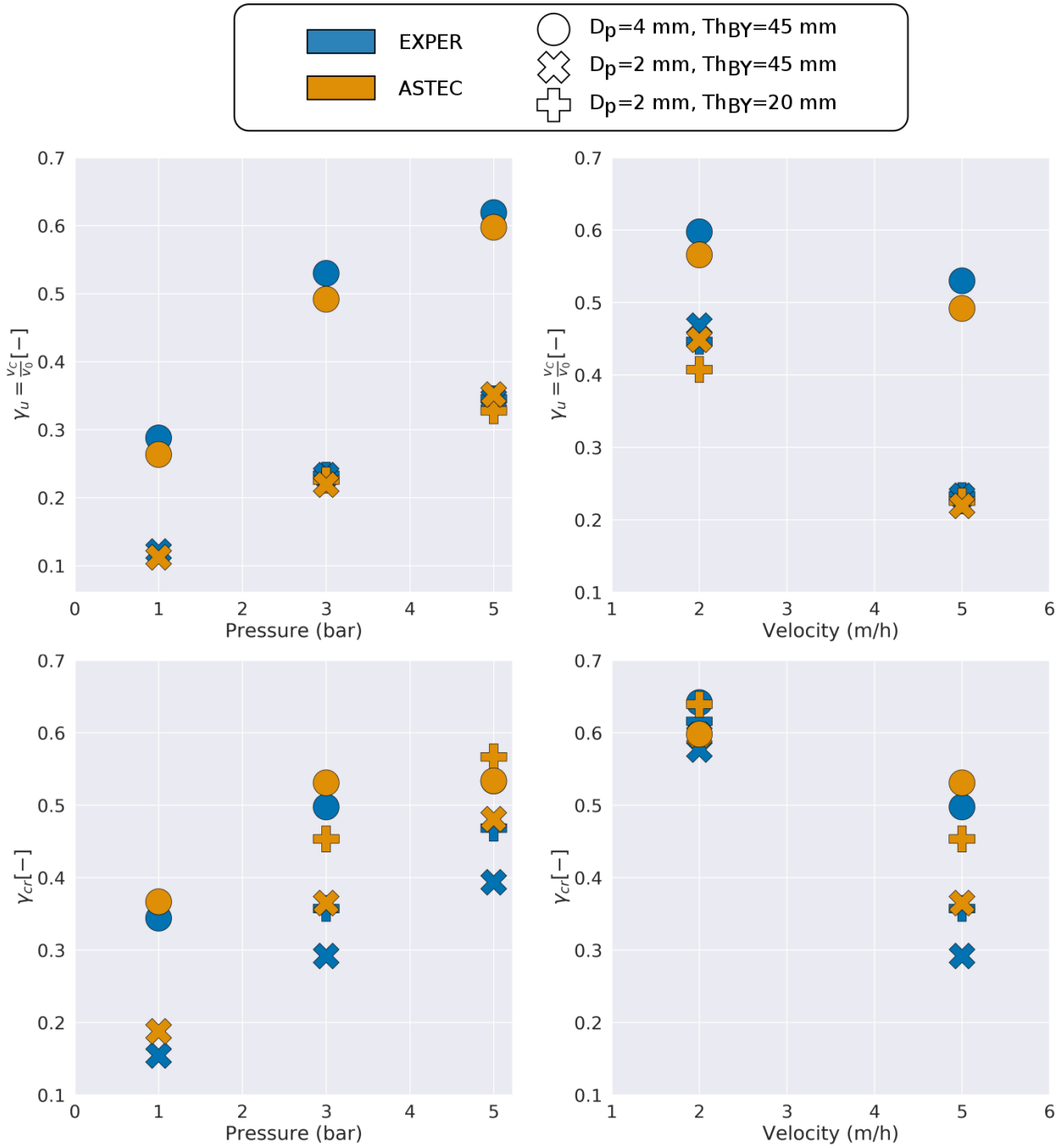
Figure 10: Experimental and Predicted quench front velocity ratio (γ_u) and conversion ratio (γ_{cr}) as a function of the system pressure (injection velocity of 5 m/h) and the injection velocity (system pressure of 3 bar) for different bed configurations. Initial debris temperature of 700 °C in all cases.

5 Discussion

5.1 The role of capillarity

Several validation studies on core reflooding have been conducted, but the influence of capillarity has rarely been considered in the calculations. In particular, simulations using the codes MEWA

(Huang and Ma, 2018) and MC3D (Mutelle et al., 2017; Raverdy et al., 2017) obtained a correct description of the experimental results on debris beds with $D_p > 4$ mm without considering the influence of capillarity. This is reasonable, given the negligible influence of this physical mechanism for those particle sizes. However, it may be that capillarity starts to play an important role when $D_p < 2$ mm. Therefore, this section studies the influence of capillarity on the shape of the computational and experimental quench front progressions.

For that aim, a capillarity correction model is introduced in the momentum equation: within each mesh, the pressure difference between the two phases (also named as the capillary pressure P_c) is given by Eq. 11, where θ is the contact angle between the liquid-gas-solid phases and $J(s)$ is the Leverett function (Leverett, 1941), which in this case is a function of the void fraction.

$$P_c = P_G - P_L = \sigma \cdot \sqrt{\frac{\varepsilon}{K}} \cdot cos\theta \cdot J(\alpha)$$
<div align="right">Eq. 11</div>

For the study on capillarity, the quench front progression associated with the tests PA-2 and D5-2 is investigated. Two bounding computational cases are considered: PCAP=OFF, without considering the capillarity correction, represent the reference results obtained during the validation (section 4); PCAP=ON represent the computational results considering the capillarity correction at its maximum ($\theta=0°$). Experimental and computational results are shown in Figure 11 for tests PA-2 and D1-7, which only differ by the particle size.
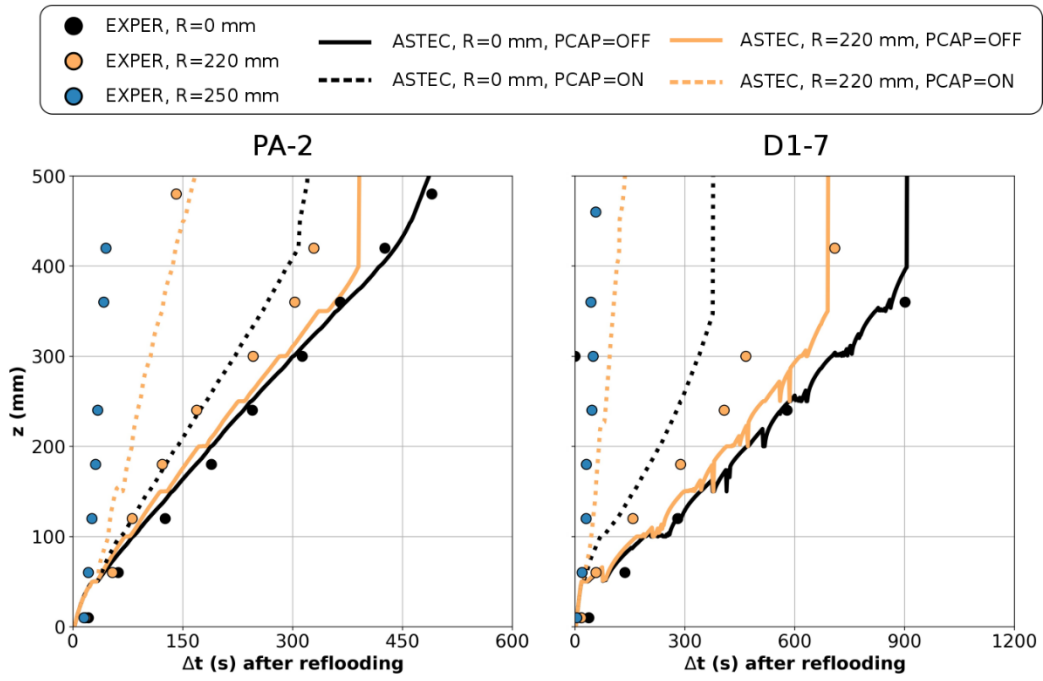
Figure 11: Predicted vs. Experimental evolution of the quench front for the tests PA-2 and D1-7 (see Table 1) with and without the capillarity correction.

It is observed that the consideration of capillarity correction increases the multi-dimensional effects within the main bed, but at the same time it leads to a faster quench front progression, especially in the outermost channels. Therefore, it is interesting to study the radial redistribution of steam and water near the quench front. Previous studies have shown that the radial redistribution in a two-layered porous medium takes place over the first two thirds of the redistribution height, the latter value being 0.333 m for a 0.5 m height debris bed (Swaidan, 2018). Hence, the redistribution in the PEARL debris bed should take place over 200 mm above the quench front, this being equivalent to four axial meshes of the current geometrical model. Consequently, redistribution rates for each phase are calculated by adding the radial flow rates across the interface C-BY along the first four meshes above the quench front one i.e. between IQF and IQF+4 (see Figure 12). It has been verified that this value is representative of the whole radial interface between the central bed and the bypass. Predictions with and without capillarity correction can be found in Figure 13 for the test PA-2.
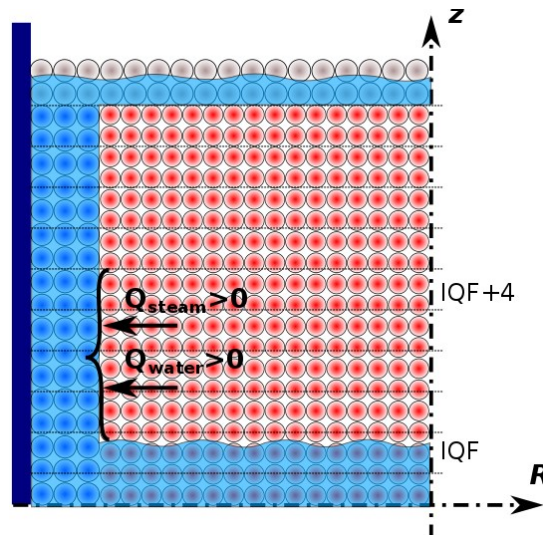

Figure 12: Sketch representing the redistribution of water/steam from the central bed towards the bypass (>0).
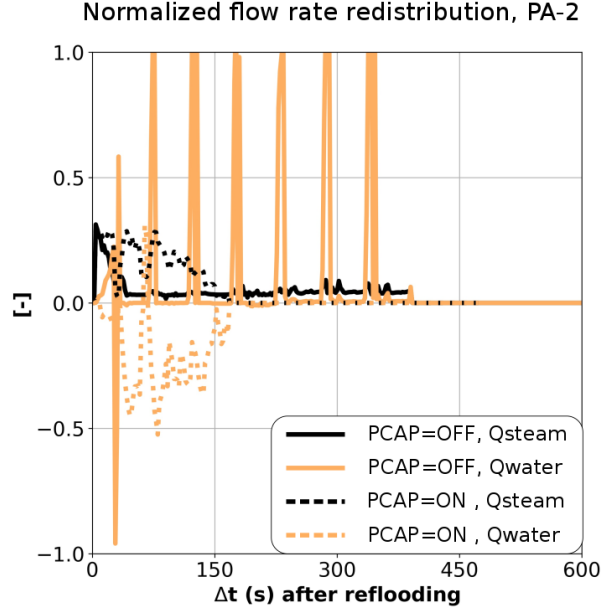
Figure 13: Normalized steam/liquid radial redistribution predicted by ASTEC along the interface C-BY for the test PA-2 with/without capillarity correction. Normalization performed with the injected water flow rate.

The consideration of capillarity correction leads to a simultaneous prediction of a negative liquid flow rate and a positive steam flow rate during the first 150 s. This means that the liquid is transferred from the bypass to the central bed in the quench front vicinity, even if the steam is flowing in the opposite direction. In contrast, neglecting the capillary correction prevents the liquid from entering the main bed and enhances water redistribution towards the bypass as the quench front moves to a new mesh. In order to understand this, the ASTEC V2.1 momentum conservation equations at the interface C-BY of the mesh IQF+2 are written at a time when steam redistribution is taking place for the gas and liquid phases (Eq. 12 and Eq. 13). Therein, the interfacial friction term is neglected due to its minor importance in the radial redistribution (this is explained in section 5.2).

$$- \alpha \, \nabla P_G = F_{\mu,G} \boldsymbol{v_G} + F_{\eta,G} \boldsymbol{v_G} \boldsymbol{v_G} \qquad \text{Eq. 12}$$

$$-(1 - \alpha) \nabla P_L = F_{\mu,L} \boldsymbol{v_L} + F_{\eta,L} \boldsymbol{v_L} \boldsymbol{v_L} \qquad \text{Eq. 13}$$

According to the result of this section, steam is redistributed towards the bypass, while water is being transferred to the main bed. This means that the first term of Eq. 12 is positive, while the first term of Eq. 13 is negative. The term $-\nabla P_L$ can also be written as the difference between the liquid pressure in the central bed (P_L^C) and the bypass (P_L^{BY}), which can also be expressed as a function of the gas pressure in the central bed (P_G^C) and bypass (P_G^{BY}) and the corresponding capillarity corrections.

24

$$-\nabla P_L \propto (P_G^C - P_G^{BY}) - (P_c^C - P_c^{BY}) \qquad \text{Eq. 14}$$

Since the pressure gradient of the gas phase is positive, this means that the capillarity correction is responsible for the sign modification of the liquid pressure gradient. This is occurring because of the large gradient of void fraction between the bypass and the external part of the central bed, which is related to the low permeability of the debris bed in the bypass. In turn, water is transferred towards the innermost channel of the main bed because of the hydrostatic pressure head, thereby creating a curved quench front profile within the main bed.

Coming back to the comparison between predictions and experiment, the experimental quench front progression observed in PA-2 is better predicted if the capillarity correction is not considered, which is justified given its negligible influence for $D_p > 4$ mm. Conversely, taking into account the capillarity correction leads to multi-dimensional quenching front as observed in D1-7. However, if the current model for the capillarity pressure correction is considered, there is a strong water absorption by the main bed whatever the value of wetting angle θ (not shown in the article), which leads to an overestimation of the conversion ratio and a faster quenching of the main bed. This shows that further investigations in the modelling of capillarity are required to correctly describe the phenomena especially for particle beds with $D_p < 2$ mm.

It is worthwhile mentioning that ASTEC predictions obtained on PA-2 when considering capillarity correction are similar to those obtained by ICARE-CATHARE calculations (Swaidan, 2018), which, by default, included the same capillary correction model. In that study, the steam generation rate falls down to zero at about 350 s, which is congruent with the results predicted by ASTEC when capillarity is considered (see the arrival of the quench front of the main bed to the top in Figure 11).

5.2   Redistribution and water entrainment in the bypass

There has been some discussion about the physical mechanisms favoring the redistribution of steam and the acceleration of liquid along the bypass i.e. water entrainment. After a careful observation of the experimental results (Chikhi et al., 2017; Chikhi and Fichot, 2017), it was stated that the main cause for steam redistribution towards the bypass could be the large radial pressure gradient originated within the bed near the quench front, whereas the main cause for water entrainment along the bypass could be the interfacial drag forces between the gas and liquid phases.

However, calculations have not provided a wide consensus on those mechanisms. Indeed ICARE-CATHARE calculation on PEARL tests show the importance of lateral steam and water flows in the

vicinity of the quench front to explain the experimental results (Chikhi et al., 2017; Swaidan, 2018), whereas MC3D calculations state that these lateral flows have a rather weak influence on the quench front progression (Raverdy et al., 2017). Therein, the authors stated that the inclusion of a "virtual" adiabatic plate (in the calculation) between the bypass and the bed had a limited impact on the simulation results. However, it is also true that the addition of the plate led to a decrease of steam generation in contrast to the calculations without the plate. This indicates that the large axial pressure gradient originated within the central bed slowed down the axial quench front progression in presence of a vertical plate, the steam leaving the top of the central bed, whereas in the second case the steam was partially diverted towards the bypass. Therefore, lateral flows may not be negligible after all.

Concerning water entrainment, the authors in (Chikhi et al., 2017) made several ICARE-CATHARE calculations on selected PEARL tests without explicitly considering the interfacial drag between the liquid and gas phases. Therein, the authors stated that the addition of an interfacial drag force term had a limited impact on water entrainment. However, those simulations included a capillary correction, which – as we showed in the previous section - weakened water entrainment. More recently, an analytical model of flow redistribution in a two-layered porous medium (Swaidan, 2018) showed that water entrainment along the bypass could only be obtained when either (Schulenberg and Müller, 1987; Tung and Dhir, 1988) interfacial drag models were included in the description of the pressure losses.

Bearing these considerations in mind, the validated ASTEC V2.1 reflooding model is applied to PA-2 to shed light on the key physical mechanisms affecting steam redistribution and water entrainment. Twenty axial meshes instead of ten are considered within the bed to gain better insights. Figure 14 focuses on the radial behavior at the interface between bed and bypass: the left-hand side shows the radial steam flow rate profile along the interface, whereas the right-hand side shows the different terms involved in the momentum conservation equation of the gas phase along such interface: total pressure gradient (involving hydrostatic pressure gradient), regular friction and interfacial friction terms. The temporal term has not been included since the profile is drawn at a time when quasi-steady state is established. Conversely, Figure 15 focuses on the axial behavior along the bypass: the left-hand side shows the axial liquid velocity, whereas the right-hand side shows the liquid momentum conservation terms along the bypass.
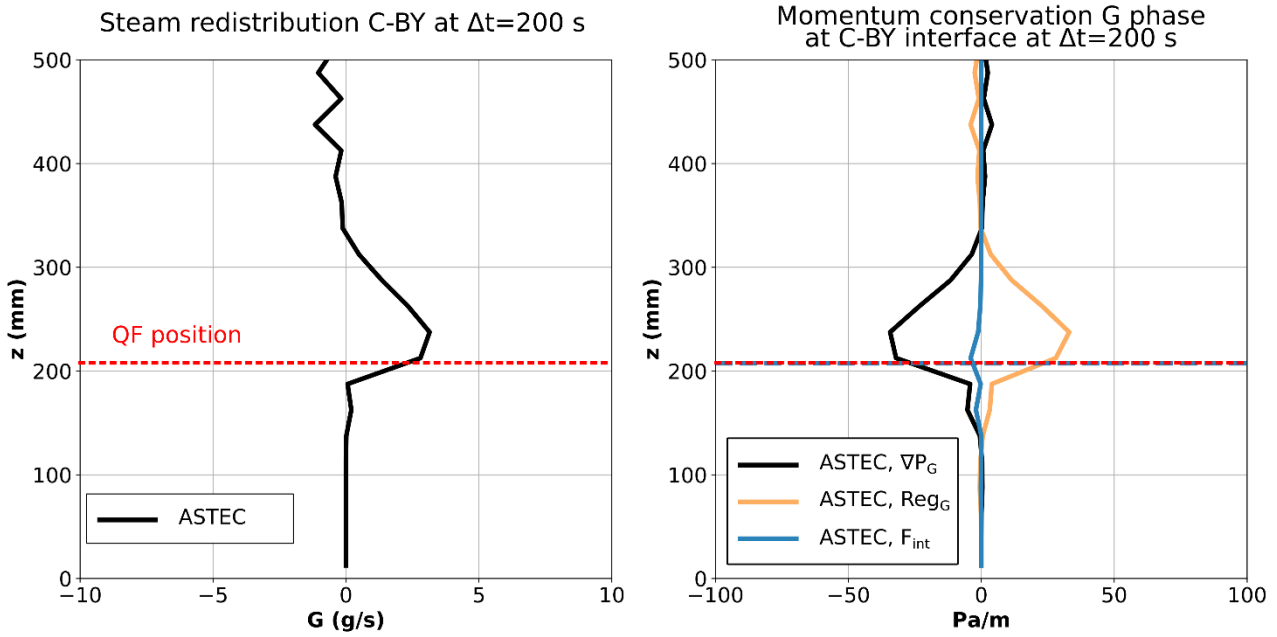
Figure 14: Predicted radial steam redistribution and momentum conservation profile for the gas phase at the radial interface central bed - bypass for the test PA-2. Profiles are depicted 200 s after reflooding onset. The horizontal dashed line represents the location of the quench front in the outermost bed channel.
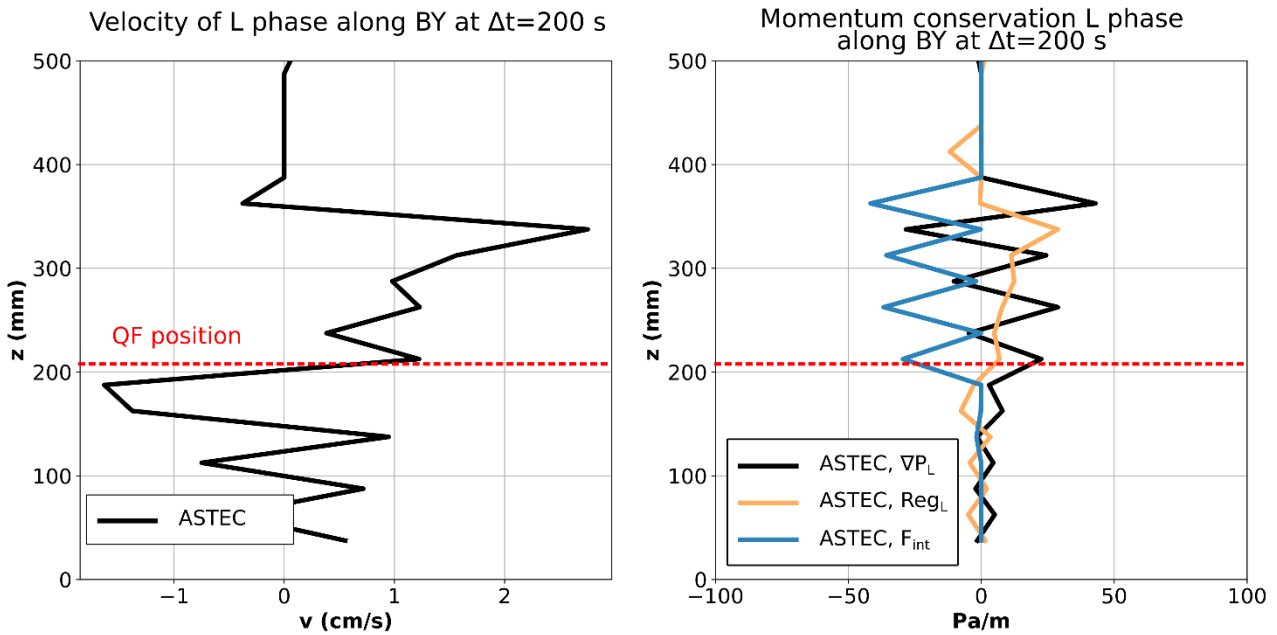

Figure 15: Predicted liquid vertical velocity and momentum conservation along the axial interfaces of the bypass for the test PA-2. Profiles are depicted 200 s after reflooding onset. The horizontal dashed line represents the location of the quench front in the outermost bed channel.

Looking at Figure 14, the radial redistribution of steam takes place along the first meshes above the quench front. The driving term of such redistribution is the radial pressure gradient, which is built up

from the significant steam production within the central bed. Besides, there is a limited contribution of the interfacial friction term to the radial momentum balance along the whole interface. Sensitivity analyses on the Schulenberg correlation for interfacial friction have been carried out by using multiplicative factors of several orders of magnitude (10 and 100), but the main term for the radial redistribution remained the pressure gradient originated within the bed. This is congruent with the experimental and computational explanations given in (Chikhi et al., 2017).

Consequently, the liquid is accelerated along the bypass region where the steam redistribution is taking place, as shown in the left-hand side of Figure 15. A quick glance to the right-hand side shows that the liquid is mainly accelerated due to the interfacial friction with the gas phase, which is coherent with the experimental explanations provided in (Chikhi et al., 2017; Chikhi and Fichot, 2017) and the results of aforementioned analytical model (Swaidan, 2018). Therefore, we can conclude that the analysis on the suitability of interfacial friction based on ICARE-CATHARE calculations (Chikhi et al., 2017) was probably overshadowed by the inclusion of the capillarity. A further analysis of Figure 15 reveals that the liquid velocity in the bypass reaches its maximum at about 150 mm above the quench front (at R=220 mm), which is consistent with the maximum elevation at which steam radial redistribution is taking place. This means that water is accelerated in the bypass as long as radial steam redistribution takes place. Downstream, the liquid velocity in the bypass decreases as a function of the elevation until it is discharged into the still upper pool.

Further calculations on other PEARL tests involving noticeable two-dimensional effects (e.g. PA-2, PA-5 and D1-7) lead to the same conclusions. They also reveal that, if radial steam redistribution takes place, the void fraction is uniform along the bypass region located above the quench front. Moreover, its value never exceeds 0.70, as illustrated for PA-2 in Figure 16. This indicates that the water can be entrained up to a limit, beyond which an increase of redistribution will no longer accelerate the water in the bypass. This is related to the increase of the gravity term of the liquid phase and the decrease of interfacial friction term driving the liquid, as the void fraction decreases.
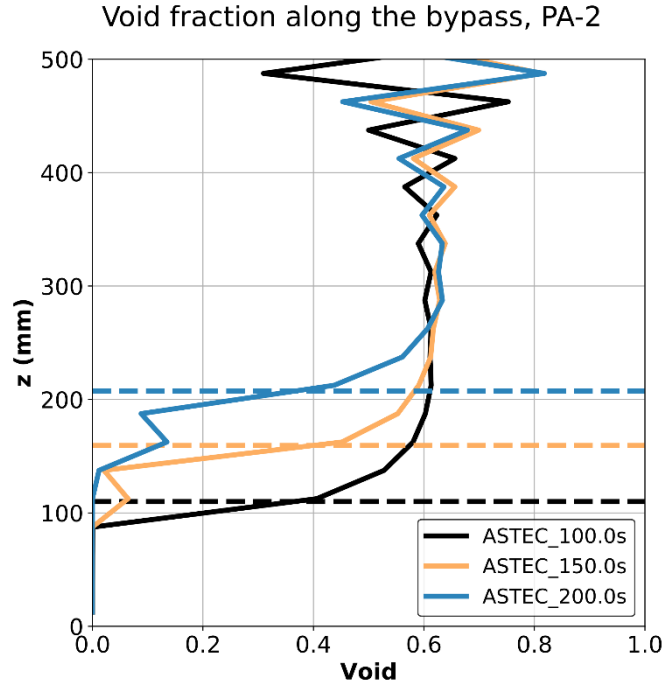
Figure 16: Predicted void fraction profiles along the bypass as a function of time for the test PA-2. Horizontal dashed lines represent the location of the quench front in the outermost bed channel at the times when the void fraction profiles are plotted.

5.3 Top flooding and second peak in steam generation rate

Hypotheses were also made about the mechanisms driving the second peak of the steam generation rate occurring for the tests involving a 2-D quench front progression e.g. PA-2. (Chikhi and Fichot, 2017) suggested that, once the quench front reaches the upper part of the heated bed, the radial pressure loss coefficient would outweigh the axial one at the last stages of reflooding, this possibly enhancing evaporation. Calculations on PEARL experiments using ICARE-CATHARE (Swaidan, 2018), MC3D (Raverdy et al., 2017) and MEWA (Huang and Ma, 2018) have not managed to give an explanation either, since the peak could not be predicted. Therefore, the origin of the second peak at the end of PEARL experiments performed on 4 mm particle beds remains still unclear.

In order to investigate the subject, the present section compares the validated ASTEC V2.1 reflooding model with the experimental results of PA-2. The temperatures of the main heated bed at R=0, 160 and 220 mm are analyzed in Figure 17. A horizontal purple line representing T_{MFB} has also been included, since this variable is used for the quench front detection method.

The experimental curves show that the debris located at R≤160 mm are bottom-quenched, even if some water enters the bed at the top. Conversely, the debris located at R=220 mm undergoes bottom

flooding for z < 360 mm and top flooding for z > 480 mm. Therefore, experimental results on debris beds with D_p=4 mm suggest that the likeliness of top flooding increases as we approach towards the external part of the heated bed. It is noticed that the hottest bed locations are quenched in the time window of 300-460 s, which is consistent with the second peak in the steam generation rate, taking place at about 400s (see Figure 5).

On the other hand, predictions show that particles located at z=480 mm are precooled and some of them even quenched (for R≥160 mm) before those located at z=420 mm, which indicates the occurrence of top flooding. Comparing the predicted quench front evolution and bed temperatures at R=220 mm for PA-2, we observe a time shift between the arrival of the quench front at the top of the bed (390 s, see Figure 4) and the quenching of debris particles (470 s, see Figure 17). It is also noticed that the second peak of the steam generation rate coincides with the quenching of debris particles located within R=160-220 mm.

Such a time shift is related to the second hypothesis used in the quench front detection method (see section 2.3), which stated that a quench front could be detected in the mesh IQF if the temperature of the debris located in the mesh IQF+1 was above T_{MFB}. Indeed, such a condition is not satisfied for R=160 mm when the front reaches z=420 mm (IQF), since the debris at z = 480 mm (IQF+1) has already been top quenched. Therefore, the debris at R=160 mm and z=420 mm are cooled down at a slower pace, since the heat flux is calculated according to film boiling regime, which is much lower than that of transition boiling (see section 2.3). This explains the sink in the steam generation rate at 400 s in PA-2 (see Figure 5). The film boiling regime applies until the temperature falls below T_{MFB}, when there is a switch to nucleate boiling. At that point, the steam generation peaks, since the nucleate boiling correlation strongly depends on the surface overheating.

In conclusion, the predicted time shift between the arrival of the quench front at the top of the bed and the second peak in the steam generation rate can be ascribed to the quench front tracking method. If the violent switch between transition boiling, film boiling and nucleate boiling could be prevented, then the steam generation rate should not experience a sink. Instead, it should present a peak due to the merging of the upward and downward quench fronts in the outermost channels of the main bed. Future modifications will be introduced in the quench front detection method in order to avoid violent switches in the heat transfer. This modification may allow identifying if the second peak, characteristic of certain experiments of Bed 1, can be ascribed to the collapse of the downward/upward quench front between R=160 mm and R=220 mm. If this is eventually the reason,

this could also explain why a second peak in the steam generation rate was not observed in Bed 2-1 and 2-2 (i.e. lack of top flooding).
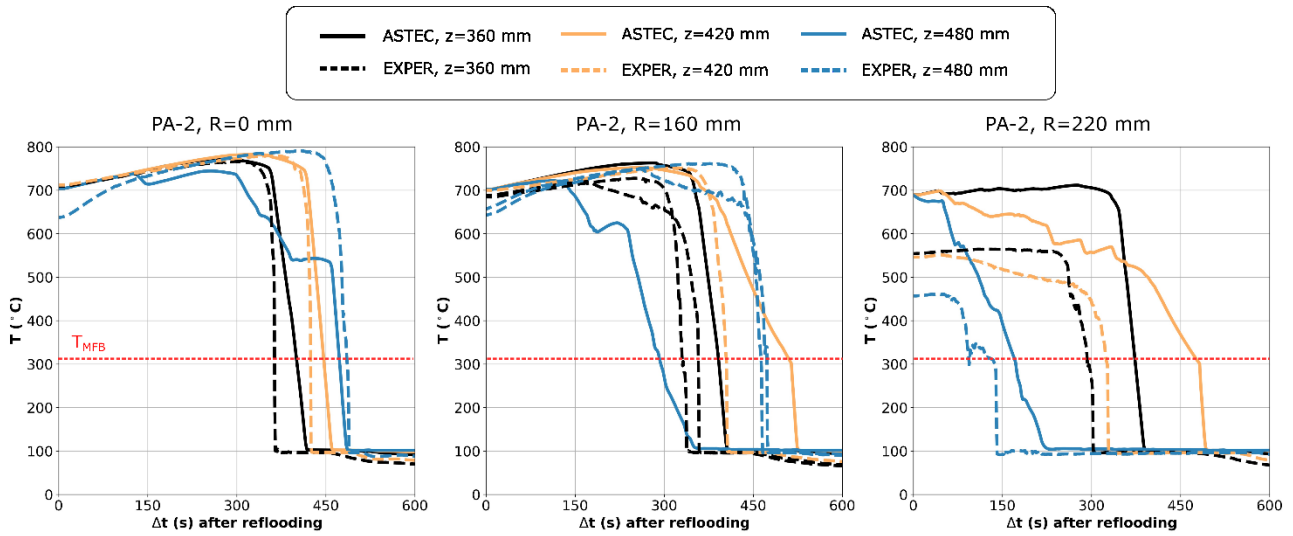

Figure 17: Evolution of computational (without capillarity) and experimental debris temperatures at selected radial and axial locations for the test PA-2. Red horizontal line represents the minimum film boiling temperature. Two experimental lines of the same kind indicate measurements at two different azimuthal positions.

6 Conclusions

A reflooding model for debris bed geometries has been implemented in ASTEC V2.1. It is consistent and compatible with the model already implemented for intact fuel assemblies (Gomez-Garcia-Torano and Laborde, 2021). This has been possible thanks to several developments:

- Dynamic calculation of the debris and rod surface for each mesh by CESAR. Depending on such ratio, the fluid friction configuration is considered as bundle or porous. Junctions interconnecting two meshes are considered porous when at least one mesh is porous.

- In porous junctions, replacement of one momentum equation on mean velocity (associated with the drift approach) by a set of two momentum equations on gas and liquid velocities with specific porous friction terms.

- Unification of the reflooding heat-transfer model whatever the core degradation state (intact, partially, or severely degraded): the same quench front detection method is applied whatever the degradation state. Besides, the same correlations are applied to describe the parietal heat flux in the quench front vicinity.

As far as debris beds are concerned, the model was validated using data from the PEARL experimental facility representative of a hypothetical debris bed in a 1300 MWe PWR. The current study has considered bottom flooding tests involving a wide range of pressures, injection velocities, particle diameters and bypass thicknesses. Generally, the model can adequately predict conversion ratio and quench front velocity ratio for tests involving either a one or multi-dimensional quench front progression. However, qualitative deviations start to appear as the system pressures decrease and the injection velocities increase for 2 mm particle beds. For those situations, the quench front progression velocity is clearly underestimated across the main bed, but this is compensated by an enhanced redistribution towards the bypass and top flooding, which was not detected in the experiment. This raises questions about the modelling of capillarity when dealing with the reflooding of a two-layered heated porous media with different permeability in severe accident codes.

Following the comparison of experimental and computational results, further insights have been gained regarding the coolability of degraded cores, quantified in relative terms by the quench front velocity ratio and the conversion ratio:

- For a given debris bed geometry, coolability is enhanced for increasing system pressures and decreasing mass flow rates. For given thermalhydraulic conditions at injection time, coolability is enhanced when the bed consists of coarse fragments and it is surrounded by large permeable zones. It is reminded that, even if the quenching time of a debris bed decreases with increasing mass flow rate, the coolability is reduced in relative terms.

- For the opposite conditions (i.e. low system pressures, increasing mass flow rates, tiny fragments and narrow permeable zones), steam is redistributed towards the bypass and possibly entrains a part of the water, this eventually leading to lower availability of water within the bed. It must be noticed that, in such a case, the actual residual power will heat up the regions above the core and possibly lead to the creation of molten pools, which may hinder coolability.

- The reduction of the particle diameter leads to an increasing heterogeneity in the radial quench front profile due to the increasing absorption of water by capillarity in the main bed.

- The additional reduction of the bypass thickness enhances steam generation but does not affect quenching times. In those cases, the cooling efficiency is increased, since more steam is produced for the same mass of injected liquid.

- Code calculations suggest that such a radial redistribution is mainly driven by the large pressure gradients created within the bed, whereas water entrainment along the bypass is

mainly driven by the interfacial friction. They also suggest that there is a threshold beyond which the water entrainment cannot be significantly increased.

- The peak of steam generation at the end of reflooding could be related to the collapse of the downward and upward quench front, but this needs to be verified after implementing further modelling modifications in the quench front tracking method.

The development of a validated comprehensive reflooding model valid regardless the degradation state is significant in terms of Severe Accident Management, where one of the key aspects is to know if an injection system may succeed in quenching the degraded core. Knowing that the code provides a reliable prediction of reflooding, deterministic analyses on risk-significant accidental sequences can be carried out in order to characterize a successful injection and the most appropriate safety systems for such aim. In parallel, it is also worthwhile to further develop existing analytical models to characterize the transition between a one-dimensional and multi-dimensional quench front progression.

Nomenclature

Acronyms:

- IQF   Quench front mesh
- QF   Quench front
- SAM   Severe Accident Management

General variables

- d_p: particle diameter
- F_i : interfacial drag (N/m^3)
- g: gravitational acceleration, 9.81 m/s^2
- j_k: superficial velocity (m/s)
- $J(s)$: Leverett function (-)
- K: permeability (m^2)
- K_i: relative permeability (-)
- P_k: Pressure (Pa)
- P_c: Capillary pressure (Pa)
- R: Radial coordinate (m)
- T: temperature (K)
- Th_{BY}: Bypass thickness (m)
- v_k: interstitial velocity (m/s)
- z: axial coordinate (m)

Greek letters:

- α: void fraction (-)
- γ_{cr}: conversion ratio (-)
- γ_u: quench front velocity ratio (-)
- ε: porosity (-)
- η: passability (m)
- η_k: relative passability (-)
- θ: contact angle (rad)
- μ_k: dynamic viscosity (Pa s)
- ρ_k: density (kg/m^3)
- σ: surface tension (N/m)

Indices:

- BY: bypass
- C: central bed
- k: fluid phase (L: liquid (water), G: gas (steam))
- 0: inlet condition at the bottom of the bed
- sat: saturation
- mfb: minimum film boiling
- w: wall
- inj: relative to injection

Acknowledgements

References

Akers, D., Carlson, E., Cook, B., Ploger, S., Carlson, J., 1986. TMI-2 Core Debris Grab Samples Examination and Analysis. Sandia National Laboratory GEND-INF-075.

Bachrata, A., 2012. Modélisation du renoyage d'un cœur du réacteur nucléaire fortement dégradé. Université de Tolouse.

Bachrata, A., Fichot, F., Repetto, G., Quintard, M., Fleurot, J., 2013. Quench Front Progression in a Superheated Porous Medium: Experimental Analysis en Model Development. J. Energy Power Eng. 7, 514–523.

Berenson, P., 1961. Film boiling heat transfer from an horizontal surface. J. Heat Transfer 83, 351–358. https://doi.org/doi:10.1115/1.3682280

Bestion, D., 2011. System Code Models and Capabilities, in: THICKET 2008 – Session III. Pisa,

Italy, May 5–9, pp. 81–106.

Broughton, J.M., Kuan, P., Petti, D.A., Tolman, E.L., 1989. A Scenario of the Three Mile Island Unit 2 Accident. Nucl. Technol. 87, 34–53. https://doi.org/10.13182/NT89-A27637

Chatelard, P., Belon, S., Bosland, L., Carénini, L., Coindreau, O., Cousin, F., Marchetto, C., Nowack, H., Piar, L., Chailan, L., 2016. Main modelling features of the ASTEC V2.1 major version. Ann. Nucl. Energy 93, 83–93. https://doi.org/10.1016/j.anucene.2015.12.026

Chatelard, P., Reinke, N., Arndt, S., Belon, S., Cantrel, L., Carenini, L., Chevalier-Jabet, K., Cousin, F., Eckel, J., Jacq, F., Marchetto, C., Mun, C., Piar, L., 2014. ASTEC V2 severe accident integral code main features, current V2.0 modelling status, perspectives. Nucl. Eng. Des. 272, 119–135. https://doi.org/10.1016/j.nucengdes.2013.06.040

Chikhi, N., Clavier, R., Laurent, J.P., Fichot, F., Quintard, M., 2016. Pressure drop and average void fraction measurements for two-phase flow through highly permeable porous media. Ann. Nucl. Energy 94, 422–432. https://doi.org/10.1016/j.anucene.2016.04.007

Chikhi, N., Fichot, F., 2017. Experimental and theoretical study of large scale debris bed reflood in the PEARL facility. Nucl. Eng. Des. 312, 48–58. https://doi.org/10.1016/j.nucengdes.2016.05.009

Chikhi, N., Fichot, F., 2010. Reflooding model for quasi-intact rod configuration: Quench front tracking and heat transfer closure laws. Nucl. Eng. Des. 240, 3387–3396. https://doi.org/10.1016/j.nucengdes.2010.07.011

Chikhi, N., Fichot, F., Swaidan, A., 2017. Effect of water entrainment on the coolability of a debris bed surrounded by a by-pass: Integral reflood experiments and modelling. Ann. Nucl. Energy 110, 418–437. https://doi.org/10.1016/j.anucene.2017.06.033

Cho, D.H., Armstrong, D.R., Chan, S.H., 1984. On the Pattern of Water Penetration into a Hot Particle Bed. Nucl. Technol. 65. https://doi.org/10.13182/NT84-A33369

Coindreau, O., Fichot, F., Fleurot, J., 2013. Nuclear fuel rod fragmentation under accidental conditions. Nucl. Eng. Des. 255, 68–76. https://doi.org/10.1016/j.nucengdes.2012.09.021

Dhir, V.K., 1983. On the Coolability of Degraded LWR Cores. Nucl. Saf. 24, 319–337.

Ginsberg, T., Klein, J., Klages, J., Sanborn, Y., Schwarz, C.E., Chen, J.C., Wei, L., 1986. An experimental and analytical investigation of quenching superheated debris beds under top-reflood conditions. NUREG/CR-4493.

Glantz, T., Taurines, T., Belon, S., De Luze, O., Guillard, G., Jacq, F., 2018. DRACCAR: A multi-physics code for computational analysis of multi-rod ballooning, coolability and fuel relocation during LOCA transients. Part One: General modeling description. Nucl. Eng. Des. 339, 202–214. https://doi.org/10.1016/j.nucengdes.2018.08.031

Gomez-Garcia-Torano, I., Laborde, L., 2021. Modelling reflooding of intact core geometries in ASTEC V2.1: Improvements and validation on PERICLES experiments. Nucl. Eng. Des. 378, 111157. https://doi.org/10.1016/j.nucengdes.2021.111157

Gomez-Garcia-Torano, I., Laborde, L., Zambaux, J.A., 2018. Overview of the CESAR thermalhydraulic module of ASTEC V2.1 and selected validation studies, in: Proceedings of the 18th International Youth Nuclear Congress. Bariloche, Argentina, pp. 2–5.

Hering, W., Homann, C., Stuckert, J., 2015. Integration of New Experiments into the Reflood Map, in: Proceedings of the 15th International Congress on Advances in Nuclear Power Plants (ICAPP-15). pp. 1420–1428. https://doi.org/10.5445/IR/170100914

Hermsmeyer, S., Iglesias, R., Herranz, L.E., Reer, B., Sangiorgi, M., 2014. Review of current Severe

Accident Management (SAM) approaches for Nuclear Power Plants in Europe requirements. https://doi.org/10.2790/38824

Huang, Z., Ma, W., 2018. Numerical investigation on quench of an ex-vessel debris bed at prototypical scale. Ann. Nucl. Energy 122, 47–61. https://doi.org/10.1016/j.anucene.2018.08.018

Klein-Heßling, W., Sonnenkalb, M., Jacquemain, D., Clément, B., Raimond, E., Dimmelmeier, H., Azarian, G., Ducros, G., Journeau, C., Puebla, L.E.H., Schumm, A., Miassoedov, A., Kljenak, I., Pascal, G., Bechta, S., Güntay, S., Koch, M.K., Ivanov, I., Auvinen, A., Lindholm, I., 2014. Conclusions on severe accident research priorities. Ann. Nucl. Energy 74, 4–11. https://doi.org/10.1016/j.anucene.2014.07.015

Leininger, S., Kulenovic, R., Rahman, S., Repetto, G., Laurien, E., 2014. Experimental investigation on reflooding of debris beds. Ann. Nucl. Energy 74, 42–49. https://doi.org/10.1016/j.anucene.2014.07.007

Leverett, M.C., 1941. Capillary Behavior in Porous Solids. Trans. AIME 142, 152–169. https://doi.org/10.2118/941152-G

Magallon, D., 2009. Characteristics of corium debris bed generated in large-scale fuel-coolant interaction experiments. Nucl. Eng. Des. 236, 1998–2009. https://doi.org/10.1016/j.nucengdes.2006.03.038

Mutelle, H., Fichot, F., Piar, L., 2017. Reflooding of Large Scale Debris Bed With Bypass: Effect of Pressure and Water Flowrate, in: Proceedings of the 17th International Meeting on Nuclear Reactor Thermalhydraulics (NURETH-17). Xian, China.

Nowack, H., Chatelard, P., Chailan, L., Hermsmeyer, S., Sanchez, V., Herranz, L., 2018. CESAM – Code for European severe accident management, EURATOM project on ASTEC improvement. Ann. Nucl. Energy 116, 128–136. https://doi.org/https://doi.org/10.1016/j.anucene.2018.02.021

Raverdy, B., Meignen, R., Piar, L., Picchi, S., Janin, T., 2017. Capabilities of MC3D to investigate the coolability of corium debris beds. Nucl. Eng. Des. 319, 48–60. https://doi.org/10.1016/j.nucengdes.2017.04.005

Schäfer, P., Groll, M., Kulenovic, R., 2006. Basic investigations on debris cooling. Nucl. Eng. Des. 236, 2104–2116. https://doi.org/https://doi.org/10.1016/j.nucengdes.2006.03.033

Schanz, G., Hagen, S., Hofmann, P., Schumacher, G., Sepold, L., 1992. Information on the evolution of severe LWR fuel element damage obtained in the CORA program. J. Nucl. Mater. 188, 131–145. https://doi.org/10.1016/0022-3115(92)90462-T

Schulenberg, T., Müller, U., 1987. An improved model for two-phase flow through beds of coarse particles. Int. J. Multiph. Flow 13, 87–97. https://doi.org/10.1016/0301-9322(87)90009-7

Steinbrück, M., Große, M., Sepold, L., Stuckert, J., 2010. Synopsis and outcome of the QUENCH experimental program. Nucl. Eng. Des. 240, 1714–1727. https://doi.org/10.1016/j.nucengdes.2010.03.021

Swaidan, A., 2018. Study of water injection with evaporation in a heterogeneous highly degraded nuclear reactor core injection with evaporation in a heterogeneous highly degraded nuclear reactor core. Université de Toulouse.

Thom, J.R.S., Walker, W.M., Fallon, T.A., Reising, G.F.S., 1965. Boiling in Sub-Cooled Water during Flow up Heated Tubes or Annuli, in: Symposium on Boiling Heat Transfer in Steam Generation Units and Heat Exchangers. pp. 226–246. https://doi.org/10.1243/pime_conf_1965_180_117_02

Tung, V.X., Dhir, V.K., 1988. A hydrodynamic model for two-phase flow through porous media. Int.

J. Multiph. Flow 14, 47–65. https://doi.org/10.1016/0301-9322(88)90033-X

Tung, V.X., Dhir, V.K., 1987. Quenching of debris beds having a variable permeability in the axial and radial directions. Nucl. Eng. Des. 99, 275–284.

Tung, V.X., Dhir, V.K., Squarer, D., 1984. Quenching by top flooding of a heat generating particulate bed with gas rejection at the bottom, in: Proc of the Sixth Information Exchange Meeting on Debris Coolability. UCLA.

Tutu, N.K., Ginsberg, T., Klein, J., Klages, J., Schwarz, C.E., 1984. Debris bed quenching under bottom flooding conditions (in-vessel degraded core cooling phenomenology). New York.

Van Dorsselaere, J.-P., Auvinen, A., Beraha, D., Chatelard, P., E.Herranz, L., Journeau, C., Klein-Hessling, W., Kljenak, I., Miassoedov, A., Paci, S., Zeyen, R., 2015. Recent severe accident research synthesis of the major outcomes from the SARNET network. Nucl. Eng. Des. 291, 19–34. https://doi.org/https://doi.org/10.1016/j.nucengdes.2015.03.022

Wang, C.H., Dhir, V.K., 1988. An Experimental investigation of multidimensional quenching of a simulated core debris bed. Nucl. Eng. Des. 110, 61–72.